JACS
JOURNAL OF THE AMERICAN CHEMICAL SOCIETY
Article
pubs.acs.org/JACS

# Probing Oxide-Ion Mobility in the Mixed Ionic−Electronic Conductor $La_2NiO_{4+\delta}$ by Solid-State $^{17}O$ MAS NMR Spectroscopy

David M. Halat,[†] Rıza Dervişoğlu,[†,∥] Gunwoo Kim,[†] Matthew T. Dunstan,[†] Frédéric Blanc,[†,‡] Derek S. Middlemiss,[§] and Clare P. Grey*[,†]

[†]Department of Chemistry, University of Cambridge, Lensfield Road, Cambridge CB2 1EW, United Kingdom
[‡]Department of Chemistry, Stephenson Institute for Renewable Energy, University of Liverpool, Crown Street, Liverpool L69 7ZD, United Kingdom
[§]Department of Chemistry, University of Warwick, Coventry CV4 7AL, United Kingdom

Supporting Information

**ABSTRACT:** While solid-state NMR spectroscopic techniques have helped clarify the local structure and dynamics of ionic conductors, similar studies of mixed ionic−electronic conductors (MIECs) have been hampered by the paramagnetic behavior of these systems. Here we report high-resolution $^{17}O$ ($I$ = 5/2) solid-state NMR spectra of the mixed-conducting solid oxide fuel cell (SOFC) cathode material $La_2NiO_{4+\delta}$, a paramagnetic transition-metal oxide. Three distinct oxygen environments (equatorial, axial, and interstitial) can be assigned on the basis of hyperfine (Fermi contact) shifts and quadrupolar nutation behavior, aided by results from periodic DFT calculations. Distinct structural distortions among the axial sites, arising from the nonstoichiometric incorporation of interstitial oxygen, can be resolved by advanced magic angle turning and phase-adjusted sideband separation (MATPASS) NMR experiments. Finally, variable-temperature spectra reveal the onset of rapid interstitial oxide motion and exchange with axial sites at ∼130 °C, associated with the reported orthorhombic-to-tetragonal phase transition of $La_2NiO_{4+\delta}$. From the variable-temperature spectra, we develop a model of oxide-ion dynamics on the spectral time scale that accounts for motional differences of all distinct oxygen sites. Though we treat $La_2NiO_{4+\delta}$ as a model system for a combined paramagnetic $^{17}O$ NMR and DFT methodology, the approach presented herein should prove applicable to MIECs and other functionally important paramagnetic oxides.

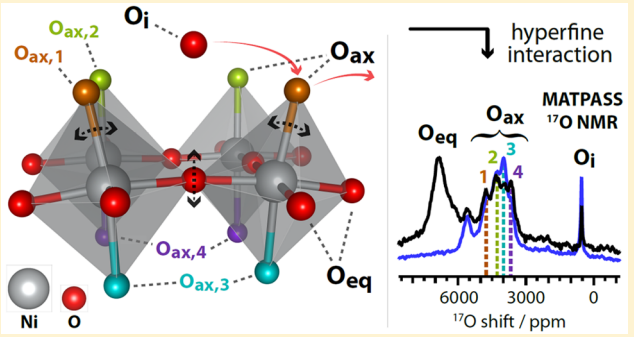


## 1. INTRODUCTION

Mixed ionic and electronic conducting (MIEC) ceramics have shown promise in recent years as oxygen-transport membranes in solid oxide fuel cells (SOFCs) and for chemical looping applications.[1−7] The use of mixed conductors, primarily perovskite-type oxides, as SOFC cathodes has been shown to improve oxygen reduction kinetics and thus enable device operation at lower temperatures.[8,9] Typically, the advanced functionality of these mixed-conducting systems derives from the mutual influence of metal cation mixed valency and oxygen nonstoichiometry.[10] While the latter property, manifesting as oxygen vacancies or interstitials, has been directly implicated in the bulk performance of MIECs, the mechanistic origins of oxide-ion conductivity often remain unclear at the atomic level. Atomistic simulations have provided insight into underlying interstitial and vacancy mediated contributions to ionic conductivity,[11] but direct experimental confirmation of these details of ionic motion remains a challenge.

Unlike conventional diffraction-based methods sensitive to long-range order, solid-state NMR spectroscopy can provide insight into local, atomic-scale distortions in solids, with direct relevance to ionic conduction.[12−15] Moreover, exchange rates and activation energies for thermally activated transport processes can be derived from NMR spectra acquired at variable temperature (VT-NMR). Our group[16−21] and others[22−30] have shown that solid-state $^{17}O$ VT-NMR in particular can enable detailed mechanistic studies of fast oxide-ion conductors, subject to successful enrichment[31,32] of samples with $^{17}O$ (natural abundance 0.037%). Moreover, as a spin-5/2 nucleus with moderate electric quadrupole moment, $^{17}O$ is sensitive to electric field gradients (EFGs) generated by local charge and bonding asymmetry, as quantified through site-specific quadrupole coupling constants ($C_Q$). This quadrupolar interaction can further discriminate among different coordination environments in diamagnetic oxides.[33]

Similar $^{17}O$ NMR studies of *paramagnetic* oxides such as MIECs, however, have met with comparatively limited

**Received:** July 16, 2016
**Published:** August 19, 2016

  

DOI: 10.1021/jacs.6b07348
J. Am. Chem. Soc. 2016, 138, 11958−11969

success.[34] In paramagnetic materials, electron−nuclear spin interactions lead to large Fermi contact (hyperfine) shifts and anisotropic dipolar broadening that complicate spectral detection, resolution and assignment. Previous reports have generally been confined to single crystal samples, with spectra often recorded at cryogenic temperatures.[35−37] In a significant advance by Kong et al., the first $^{17}$O magic-angle spinning (MAS) NMR spectra of paramagnetic transition metal complexes have been recorded and assigned.[38] In this work, we extend paramagnetic $^{17}$O MAS NMR to perform advanced pulse sequence techniques and variable-temperature measurements on a model MIEC, $La_2NiO_{4+\delta}$, to explore the structural and mechanistic details of the oxide-ion transport in this material.

$La_2NiO_{4+\delta}$, a perovskite-derived $K_2NiF_4$-type mixed ionic−electronic conductor, shows high oxygen transport across a large temperature range and is an important candidate SOFC cathode material.[39] With both paramagnetic (axial $O_{ax}$, equatorial $O_{eq}$) and diamagnetic (interstitial $O_i$) oxygen sites, the system is an elegant model for initial $^{17}$O MAS NMR studies of MIECs. (By a "paramagnetic" or "diamagnetic" site, we here refer to the presence or absence, respectively, of electron spin-bearing cations such as $Ni^{2+}$ in the local (first shell) oxygen coordination environment.)

Structurally, $La_2NiO_{4+\delta}$ is a member of the Ruddlesden−Popper family and consists of alternating $LaNiO_3$ perovskite-like layers and "$La_2O_2$" rocksalt-like layers in an offset *ABA′B′* arrangement (Figure 1a). Equatorial oxygen sites lie within the perovskite plane; axial sites bridge the layers. Incorporation of interstitial oxygen within the rocksalt layers is remarkably facile, and affords a considerable range of oxygen hyperstoichiometry ($\delta$), reported from $\delta$ = 0 to ∼0.3, with $\delta$ > 0.15 for SOFC applications.[40,41] Structural and magnetic properties are very sensitive to oxygen excess.[42,43] In this work, therefore, we consider only the highly hyperstoichiometric phases most relevant for fast oxide-ion conduction in SOFC cathodes. We first show that incorporation of interstitial oxygen leads to distinct and well-resolved displacement of axial oxygen sites, and paramagnetic $^{17}$O NMR is uniquely sensitive to these local structural distortions. Results from periodic density functional theory (DFT) calculations are integral in the interpretation of the $^{17}$O NMR spectra; the axial distortion leads to a splitting of calculated hyperfine shifts, as observed experimentally, and calculated $C_Q$ values corroborate assignment of the $O_{eq}$ and $O_{ax}$ sites.

We next perform variable-temperature NMR to probe oxide-ion dynamics associated with the orthorhombic-to-tetragonal phase transition of $La_2NiO_{4+\delta}$ reported near 150 °C. At the composition $\delta$ = 0.3, Aguadero et al. have reported the phase transition temperature $T_p$ = 132 °C.[44] We argue that this transition is directly correlated with the onset of rapid interstitial motion between 110 and 130 °C, a process for which we extract an activation energy $E_a$ = 0.59 ± 0.07 eV. In particular, fast exchange between interstitial and axial oxygen sites, as in the hypothesized interstitialcy mechanism of Chroneos et al.,[45] occurs simultaneously with the abrupt disappearance of the aforementioned local distortion. This in turn induces the disruption of the cooperative tilting of perovskite layers responsible for the long-range orthorhombic (*Fmmm*) distortion, incoherently averaging the structure to the tetragonal (*I*4/*mmm*) phase. Our proposed model of oxide-ion dynamics at these temperatures involves two coupled motional processes: (1) exchange between interstitial and axial sites and (2) "rocking" of $NiO_6$ octahedra dynamically altering the displacement of axial and equatorial sites, that together determine the observed $^{17}$O VT-NMR lineshapes. In summary, we report the first $^{17}$O MAS solid-state VT-NMR spectra of a paramagnetic oxide-ion conductor, with DFT-aided assignment of the local structure and oxide-ion dynamics, which should ultimately enable future studies of functionally relevant paramagnetic oxides by similar methods.

## 2. EXPERIMENTAL AND THEORETICAL METHODS

**2.1. Synthesis, $^{17}$O-Enrichment, and Characterization.** Samples of $La_2NiO_{4+\delta}$ were prepared by a solid-state reaction route as described previously.[46−48] Stoichiometric amounts of $La_2O_3$ (Alfa Aesar, REacton, 99.999%; predried) and NiO (Aldrich, 99.999%) were mixed in a mortar and pestle, pressed isostatically, sintered in air at 1300 °C for 6−12 h, and ground into powder. Multiple intermediate sintering and grinding steps were repeated until phase purity was achieved, as determined by laboratory powder X-ray diffraction (Figure S1).

Samples were also prepared via a modified sol−gel (Pechini) method similar to that previously reported.[49] Stoichiometric amounts of $La(NO_3)_3{\cdot}6H_2O$ (Alfa Aesar, REacton, 99.999%) and $Ni(NO_3)_2{\cdot}6H_2O$ (Aldrich, 99.999%) were dissolved in an aqueous solution of poly(vinyl alcohol) (15% w/v; Merck, $M_w$ = 60 000), with a mole ratio of metal cations to hydroxyl groups in poly(vinyl alcohol) of approximately 1:3. Continuous heating at 100 °C produced a viscous green xerogel which was subsequently heated to autoignition at 400 °C. The resulting off-black powder was pressed isostatically and sintered in air at 1300 °C for 12 h. Sol−gel-synthesized samples did not differ appreciably in phase purity or excess oxygen content from samples obtained via the solid-state reaction route.

Samples of $^{17}$O-enriched $La_2NiO_{4+\delta}$ were obtained by heating the as-synthesized powder (0.1−0.3 g) to 1000 °C under an atmosphere of 70% $^{17}O_2$ (Cambridge Isotope Laboratories, used as received) in a sealed quartz tube for 24 h. Samples were slowly cooled (1 °C min) from the enrichment temperature to maximize uptake of $^{17}$O.

Phase purity of all samples was determined with powder X-ray diffraction (XRD) using a Panalytical Empyrean X-ray diffractometer equipped with a Cu K$\alpha$ source ($\lambda$ = 1.5406 and 1.5418 Å) and X'celerator CCD detector. Scans were performed on a spinning sample stage in reflection mode over the range $2\theta$ = 5° to 80° (step size $2\theta$ = 0.0167°). Diffraction patterns were analyzed with the X'Pert HighScore Plus software package and PDF pattern database, and Rietveld refinements were performed with the GSAS and EXPGUI software packages.[50,51]

Oxygen excess ($\delta$) in $La_2NiO_{4+\delta}$ was determined via thermogravimetric analysis (TGA) performed with a Mettler Toledo TGA/SDTA 851 thermobalance. Powder samples of 20−40 mg were placed in a 100 $\mu$L $Al_2O_3$ crucible and heated to 900 °C (at 3 °C min$^{-1}$) under a reducing atmosphere of 5% $H_2$ in $N_2$ (50 mL min$^{-1}$). Raw mass data collected during the heating profile were corrected from blank experiments and smoothed subject to a local regression (LOESS) algorithm. Sample nonstoichiometry was calculated as the ratio of mass losses during the two discrete reduction steps (Figure S2), where we assumed these mass losses correspond to the reactions

$$La_2NiO_{4+\delta} + \delta H_2 \rightarrow La_2NiO_4 + \delta H_2O \quad (1)$$

$$La_2NiO_4 + H_2 \rightarrow La_2O_3 + Ni + H_2O \quad (2)$$

which were driven to completion given the gas flow conditions.[52]

**2.2. Solid-State NMR Spectroscopy.** Solid-state $^{17}$O MAS NMR experiments were carried out on 7.05 T Bruker Avance II and Avance III 300 MHz spectrometers using a Bruker 4 mm HX probe (Figures 1 and 5); a 4.7 T Bruker Avance III 200 MHz using a Bruker 1.9 mm HX probe (Figure 3); and a 16.4 T Bruker Avance III 700 MHz spectrometer using a Bruker 4 mm X probe (Figure 4). Experimental parameters for all NMR data are summarized below.

Spin−echo mapping experiments at 7.05 T were performed under a MAS frequency of 12.5 kHz using a rotor-synchronized Hahn echo


DOI: 10.1021/jacs.6b07348
J. Am. Chem. Soc. 2016, 138, 11958−11969

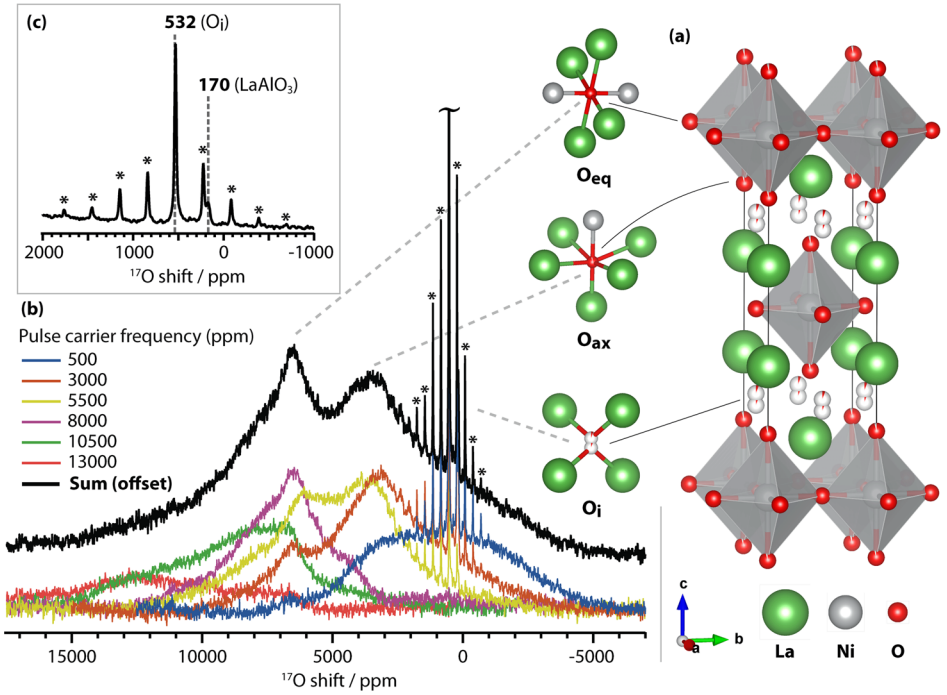


**Figure 1.** Room-temperature $^{17}O$ MAS NMR spectrum of $La_2NiO_{4+\delta}$ with proposed assignments. (a) Crystal structure of the high-temperature tetragonal (space group $I4/mmm$) phase of $La_2NiO_{4.17}$ as reported by Skinner et al.[41] Partially occupied sites ($O_{ax}$, $O_i$) are depicted as partially filled spheres. (b) Individual subspectra collected at different offset frequencies (colored) summed to give the broadband spin−echo mapping spectrum (black). Proposed assignments depict the local geometry about each oxygen environment (equatorial $O_{eq}$, axial $O_{ax}$, and interstitial $O_i$). A rotor-synchronized Hahn echo pulse sequence ($\pi/6-\tau-\pi/3-\tau-$acquire) was used for each subspectrum. Spectra were collected at 7.05 T at a MAS rate of 12.5 kHz, with 120 000 scans per subspectrum and a recycle delay of 0.5 s. Asterisks denote spinning sidebands. (c) Inset showing the "diamagnetic region" of the summed spin−echo mapping spectrum in (b). Features at 532 and 170 ppm are assigned to interstitial oxygen ($O_i$) in $La_2NiO_{4+\delta}$, and a $LaAlO_3$ impurity phase, respectively. Asterisks denote spinning sidebands.

pulse sequence of the form $(\pi/6)_x-\tau-(\pi/3)_y-\tau-$acquire with a pulse length of 1.67 $\mu$s ($\pi/6$ for liquid $H_2O$) at an inherent rf field strength of ~50 kHz and a quantitative recycle delay of 0.5 s. Similar experiments at 4.7 T were carried out at a MAS frequency of 40 kHz using a pulse length of 0.75 $\mu$s ($\pi/6$ for liquid $H_2O$) at an inherent rf field strength of ~111 kHz, and a recycle delay of 20 ms. The pulse carrier frequency step size was 2500 ppm (~102 kHz at 7.05 T, ~68 kHz at 4.7 T), i.e., smaller than the rf field strength, and a total of six subspectra were acquired at 500, 3000, 5500, 8000, 10 500, and 13 000 ppm. Further spin−echo mapping experiments at 4.7 T employed longer pulse lengths of 2.2 $\mu$s ($\pi/2$ for liquid $H_2O$) at an inherent rf field strength of ~114 kHz, with identical pulse carrier frequency offsets. Finally, all other experiments not employing spin−echo mapping for broadband excitation (i.e., MATPASS or variable temperature measurements) fixed the pulse carrier frequency offset at 3000 ppm (at 7.05 and 4.7 T) or 500 ppm (at 16.4 T). Standard saturation-recovery experiments (at 7.05 T) were used to obtain $T_1$ values.

Projection magic angle turning and phase adjusted sideband separation (MATPASS) NMR experiments[53] were performed at 4.7 T and were rotor-synchronized at a MAS rate of 40 kHz. A series of five $\pi/6$ (or $\pi/2$) pulses with pulse lengths of 0.73 $\mu$s (or 2.2 $\mu$s) were employed. A total of eight $t_1$ increments were recorded in each experiment. The recycle delay was 50 ms.

Temperature calibration of the probes was performed in separate one-pulse MAS experiments at 7.05 and 16.4 T using the $^{207}Pb$ resonance of $Pb(NO_3)_2$, with an accuracy of ±5 °C.[54,55] All $^{17}O$ NMR spectra were collected on recently $^{17}O$-enriched samples packed in $ZrO_2$ rotors with Kel-F or $ZrO_2$ caps (for room temperature and variable temperature experiments, respectively). $^{17}O$ chemical shifts were externally referenced to $H_2O$ at 0.0 ppm at room temperature. NMR spectra were processed and deconvoluted with the Bruker Topspin 3.2[56] and dmfit[57] software packages.

**2.3. First-Principles Calculations.** Calculations were performed with the CRYSTAL09 linear combinations of atomic orbitals (LCAO) code[58] using the B3LYP spin-polarized hybrid exchange-correlation functional. In a two-step approach, initial experimental structures were first geometry optimized with respect to lattice parameters and atomic positions using a more limited basis set (denoted BS-I). Next, single-point energy calculations were performed with an extended basis set (BS-II) to model the core region more accurately. Relevant NMR parameters (spin density at the nuclear positions, electron−nuclear dipolar tensors, and quadrupolar coupling constants) were computed after convergence of the wave function in the second step. Full details of the BS-I and BS-II basis sets are presented in the Supporting Information (SI). For all calculations, truncation thresholds of $10^{-7}$, $10^{-7}$, $10^{-7}$, $10^{-7}$, and $10^{-14}$ were applied to the integral series for Coulomb overlap, Coulomb penetration, exchange overlap, g- and n-exchange penetration, respectively.

The experimental room-temperature orthorhombic ($Fmmm$) structure of $La_2NiO_{4+\delta}$ ($\delta$ = 0.17)[41] was used to construct a 2 × 2 × 2 57-atom supercell ($La_{16}Ni_8O_{33}$) corresponding to $\delta$ = 0.125. The supercell was tetragonal due to expansion of the orthorhombic structure by $\sqrt{2}$ along new axes equivalent to $[110]_{Fmmm}$ and $[1\bar{1}0]_{Fmmm}$. Different initial $Ni^{3+}/Ni^{2+}$ configurations were explored with only minimal changes in the final optimized geometry, electronic structure, and computed properties. $Ni^{3+}$ ions ($d^7$) were initialized in the low-spin configuration ($t_{2g}^6e_g^1$, S = 1/2), as suggested by experimental evidence;[59] calculations failed to converge in the high-spin configuration. Full structural optimizations of atomic positions and lattice parameters were performed without symmetry constraints, with convergence tolerances on the SCF cycle total energy, root-mean-square (rms) gradient, and rms displacement of $10^{-7}$ au, 0.0003 au $Å^{-1}$, and 0.0012 Å, respectively. As a consequence of lattice anisotropy, reciprocal space sampling employed a compressed 3 × 3 × 2 Monkhorst−Pack k-point mesh.


DOI: 10.1021/jacs.6b07348
J. Am. Chem. Soc. 2016, 138, 11958−11969

Two types of NMR parameters were extracted from the calculations: (1) quadrupolar coupling constants (and associated asymmetry parameters) and (2) hyperfine shifts for all oxygen sites. Quadrupolar coupling constants $C_Q = eQV_{ZZ}/h$ and asymmetry parameters $\eta_Q = \frac{V_{XX} - V_{YY}}{V_{ZZ}}$ were determined from the principal components of the calculated electric field gradient (EFG) tensor, ordered such that $|V_{ZZ}| \geq |V_{YY}| \geq |V_{XX}|$, where Q is the nuclear quadrupole moment (−25.58 mbarn for $^{17}$O, as experimentally determined[60]). Values of the electron spin density at the oxygen nuclear positions were converted to hyperfine (Fermi contact) $^{17}$O NMR shifts using a theoretical methodology outlined previously.[61,62] In brief, calculations were first performed in the ferromagnetic state by "locking" the alignment of the Ni spins, and then the system was allowed to relax in the absence of spin constraints to a ferromagnetic local minimum. Spin density values obtained from the relaxed system were then scaled to the paramagnetic regime at the temperature of the NMR experiment assuming ideal Curie−Weiss behavior. Experimental values of $\mu_{eff}$ = 2.56 $\mu_B$ and $\Theta \approx -400$ K were used, as previously reported for $La_2NiO_{4+\delta}$.[63,64]

## 3. RESULTS

**3.1. Characterization of $La_2NiO_{4+\delta}$ by XRD and TGA.** Owing to the wide range of oxygen nonstoichiometry reported for this system, samples have been carefully characterized by XRD and TGA. Calculated values of $\delta$ from TGA measurements were found to range from $\delta$ = 0.12 to 0.17 (Figure S2). The oxygen content is significantly affected by the $^{17}$O-enrichment procedure, increasing from $\delta$ = 0.12−0.14 for as-synthesized batches to $\delta$ = 0.15−0.17 following $^{17}$O-enrichment. Our work concurs with previous findings: treatment of $La_2NiO_{4+\delta}$ under high oxygen pressure leads to even more highly nonstoichiometric samples with $\delta$ as large as 0.3.[65]

As-synthesized samples are found to be phase-pure by XRD (Figure S1). Laboratory XRD data are not sufficiently sensitive to the lighter O atoms to permit refinement of low-occupancy interstitial sites. Nonetheless, changes in the lattice parameters (as refined to the room-temperature *Fmmm* structure) mirror differences in oxygen content, as previously shown.[40,47,66,67] Here, incorporation of additional interstitial oxygen in the $^{17}$O-enriched samples leads to expansion of the lattice along *c*, with concomitant decrease of the *a* and *b* lattice parameters (Figure S3). The refined lattice parameters for the $^{17}$O-enriched samples are in good agreement with Skinner[41] and also Aguadero et al.[44,65] at similar levels of oxygen excess (that is, similar values of $\delta$) determined by TGA.

Following $^{17}$O-enrichment, a weak, broad feature is observed in the XRD pattern, which is consistent with the (117) reflection of $La_4Ni_3O_{10}$ (Figure S1), suggesting that the $La_4Ni_3O_{10}$ impurity phase (estimated at ∼3 wt %) forms during the enrichment step. Aguadero et al. and Sayers et al. also note the decomposition of $La_2NiO_{4+\delta}$ into the higher-order Ruddlesden−Popper phases $La_3Ni_2O_7$ and $La_4Ni_3O_{10}$ at high temperature and under highly oxidizing conditions.[65,68] Formation of these deleterious secondary phases may impair device longevity in functional SOFCs. In our case, these phases are difficult to distinguish from $La_2NiO_{4+\delta}$ (and from each other) due to the small phase fractions and considerable overlap of XRD reflections (Figure S1c). We turn to NMR as a (potentially) more sensitive probe of the minor impurity phases as well as the local structure of the low-occupancy interstitial sites of $La_2NiO_{4+\delta}$.

**3.2. Room-Temperature NMR.** *Acquisition of Broadband Spectra.* Initial $^{17}$O MAS NMR spectra of the enriched samples (Figure 1b) reveal an extremely broad set of features spanning more than 0.5 MHz at 7.05 T, exceeding the excitation bandwidth of a single radio frequency (rf) pulse, a direct consequence of the paramagnetism of $La_2NiO_{4+\delta}$. Acquiring the complete broadband spectrum necessitates the use of "spin−echo mapping" or "variable offset cumulative spectroscopy", VOCS,[69] here performed by collecting and summing six subspectra (colored traces, Figure 1b) with progressively larger rf carrier frequency offsets (step size equal to 2500 ppm or ∼102 kHz). Pell et al. have shown that, for nonquadrupolar nuclei, spin−echo mapping under MAS achieves nearly uniform broadband excitation,[70] but no work to date has demonstrated the validity of the technique for quadrupolar nuclei such as $^{17}$O. Given the significant width of the major features in our spectra, however, any line shape distortions are likely insignificant, and the use of a short, nonselective rf pulse ensures quantitative excitation that is independent of $C_Q$. As seen in Figure 1b, the spin−echo mapped spectrum (black) comprises two very broad components centered at ∼6500 ppm and ∼3500 ppm, and a narrow peak at 532 ppm with associated spinning sideband (ssb) manifold. A minor component appears at 170 ppm (Figure 1c), but its intensity is sample-dependent (Figure S7).

*Peak Assignments.* The resonances at 532 and 170 ppm fall within the 0−1000 ppm region occupied by shifts of diamagnetic oxides. Yang et al.[71] have reported a $^{17}$O shift of the tetrahedral oxygen site in hexagonal $La_2O_3$ of 584 ppm. Given the known[72] pseudotetrahedral coordination of interstitial oxygen ($O_i$) in $La_2NiO_{4+\delta}$ (Figure 1a, bottom right), we, therefore, assign the 532 ppm feature to the interstitial oxygen environment in $La_2NiO_{4+\delta}$. We also assign the sample-dependent 170 ppm resonance to a very minor $LaAlO_3$ impurity phase (as previously reported by Bastow et al.[73]) formed during synthesis (in an alumina crucible) but not immediately apparent in the XRD data. (Conversely, the $La_4Ni_3O_{10}$ impurity seen by XRD is not observed in our initial NMR experiments, but is later resolved in later high-temperature spectra as a minor feature at ∼2400 ppm (see below).)

The highly shifted and broadened features at ∼6500 ppm and ∼3500 ppm are assigned to equatorial $O_{eq}$ and axial $O_{ax}$ sites, respectively (Figure 1a, top and middle right). These large hyperfine shifts are attributable to delocalization of unpaired electron spin density from the 3d orbitals of the $Ni^{2/3+}$ cations to the s orbitals of proximate $^{17}$O nuclei: equatorial $O_{eq}$ sites lying in the perovskite layer, with two nearby $Ni^{2/3+}$ cations at a short distance (∼1.9 Å), are expected to experience a stronger hyperfine coupling than $O_{ax}$ sites with only one directly bonded $Ni^{2/3+}$ further away (∼2.2 Å). Additional support for this assignment comes from $T_1$ relaxation measurements, being sensitive to proximity to paramagnetic centers.[74] As expected, the $T_1$ value for the assigned $O_{eq}$ site (<500 $\mu$s) is noticeably shorter than that for $O_{ax}$ (∼1 ms). Finally, experimental evidence presented in subsection 3.4 of a much larger quadrupolar coupling constant ($C_Q$) for $O_{eq}$ is in good agreement with DFT-calculated values (subsection 3.3), confirming the assignment.

We note that our assignment of the paramagnetic sites $O_{eq}$ and $O_{ax}$ in $La_2NiO_{4+\delta}$ agrees with previous static $^{17}$O NMR results of the isostructural cuprate $La_{1.85}Sr_{0.15}CuO_4$, with the higher frequency resonance assigned to equatorial oxygen in $CuO_2$ planes, and the lower frequency feature assigned to axial sites.[75,76] However, the magnitude of the Fermi contact shifts is significantly smaller in the cuprate (equatorial: 1800 ppm; axial:


DOI: 10.1021/jacs.6b07348
J. Am. Chem. Soc. 2016, 138, 11958−11969

500 ppm), presumably as a consequence of reduced spin delocalization from $Cu^{2+}$, a cation with smaller magnetic moment than $Ni^{2+}$.

*Quantification.* All subspectra in Figure 1b have been recorded using a quantitative recycle delay (500 ms, at least 5 times $T_1$ for the $O_i$ site) so as to compare intensity across different environments. To this end, we have fitted the broadband spectrum to a sum of two Lorentzian functions (justified simply because it provided the best fit) with associated satellite transition intensity for $O_{eq}$ and $O_{ax}$ and a CSA-only spinning sideband manifold for $O_i$ (Figure S4). The integrated intensity ratio of the model, $O_{eq}$:$O_{ax}$:$O_i$ = 48:47:5 ≈ 2:2:0.2, agrees with the sample stoichiometry and is suggestive of a fully stochastic (i.e., not selective) $^{17}$O-enrichment. A stochastic enrichment indirectly confirms fast ionic conduction involving all distinct oxygen sites in $La_2NiO_{4+\delta}$ at the enrichment temperature (1000 °C), as expected of a fast oxide-ion conductor. We also note that the relative integrated intensity of the $O_i$ site (~0.2) concurs reasonably well with the oxygen excess calculated by TGA (0.15−0.17) given that we have not accounted for the signal lost from the paramagnetically relaxed $O_{eq}$ and $O_{ax}$ sites during the refocusing period prior to acquisition, i.e., we have not performed a spin−spin ($T_2$) relaxation correction. (We note that the short rf pulse length of $\pi/6$ is quantitative[77,78] given the size of the $C_Q$ values as determined later.) Finally, in comparing the weak $LaAlO_3$ signal to the $O_i$ centerband intensity, we calculate the proportion of this minor impurity for this sample to be 0.7−0.8 mol %.

**3.3. DFT Calculations.** First-principles periodic DFT calculations were performed to corroborate the argument for the given peak assignment, as well as to gain additional structural insights. Our $La_{16}Ni_8O_{33}$ supercell, corresponding to $La_2NiO_{4.125}$, contains a single interstitial oxygen defect ($O_i$) within one of the two rocksalt layers (Figure S5b). Following geometry optimization, we observe the rotation of the $NiO_6$ octahedra away from the neighboring interstitial defect. Frayret et al. have also reported interstitial-induced octahedral tilting in a compositionally identical supercell, corresponding to rotation along the $[100]_{I4/mmm}$ or, equivalently, $[010]_{I4/mmm}$ axes.[79] Our tilt axes could be described as being intermediate between the $[100]_{I4/mmm}$ and $[110]_{I4/mmm}$ directions, with the former dominant. Unlike the previous work, we observe minor tilting among octahedra not directly adjacent to the interstitial defect, possibly due to cooperative contraction of the unit cell along the stacking direction (*c*-axis).

Importantly, as also shown by Frayret et al., $O_{ax}$ sites directly adjacent to $O_i$ are displaced away from the interstitial defect and slightly toward their respective Ni centers.[79] This differential displacement, correlated with proximity to the interstitial site, amounts to a splitting of the $O_{ax}$ sites into different types. On the basis of Ni−O bond lengths, four $O_{ax}$ types are identified, as depicted in Figure 2: (1) $O_{ax,1}$, which are immediately adjacent to $O_i$; (2) $O_{ax,2}$, which are located within the same rocksalt layer as $O_i$ but not adjacent to $O_i$; (3) $O_{ax,3}$, which are the oppositely positioned $O_{ax}$ sites in the $NiO_6$ octahedra containing $O_{ax,1}$; and (4) $O_{ax,4}$, which are the oppositely positioned $O_{ax}$ sites in $NiO_6$ octahedra containing $O_{ax,2}$. The $O_{ax,3}$ and $O_{ax,4}$ sites are located within the "empty" (i.e., interstitial-free) rocksalt layer and hence not directly displaced by the interstitial defect. Average Ni−$O_{ax}$ bond lengths for the split sites ($O_{ax,1}$ through $O_{ax,4}$) are 2.13, 2.16, 2.24, and 2.26 Å, respectively, as compared to the experimental value of 2.25−2.26 Å for the stoichiometric ($\delta$ = 0) compound.[72,80]

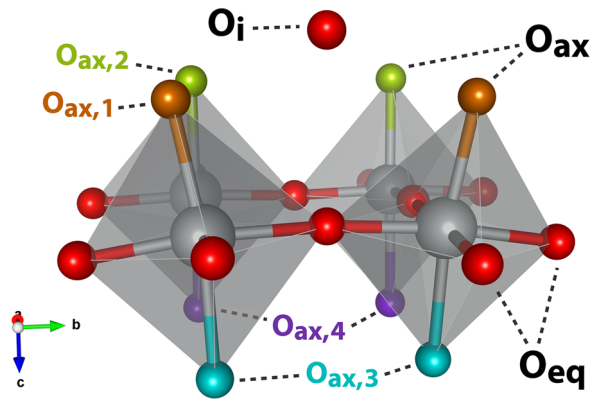


**Figure 2.** Local structural distortion induced by nearby interstitial defect ($O_i$), from part of the DFT-optimized $La_{16}Ni_8O_{33}$ supercell. Axial sites (in orange) closest to the interstitial undergo the largest displacement toward the Ni center, with concomitant tilting of the $NiO_6$ octahedra. The four types of axial oxygen sites, ordered by increasing Ni−$O_{ax}$ bond length, are depicted in orange ($O_{ax,1}$), green ($O_{ax,2}$), cyan ($O_{ax,3}$) and purple ($O_{ax,4}$). Nickel atoms are depicted in gray and nonaxial (equatorial) oxygen atoms in red. (For clarity only part of the structure is shown, omitting La.)

Although this axial distortion depends on subtle, long-range interstitial and charge ordering effects (SI, section 2), it strongly affects the calculated NMR parameters. Table 1 provides the average hyperfine shifts for equatorial, axial and interstitial sites. For each of the four $O_{ax}$ types (labeled $O_{ax,1}$ through $O_{ax,4}$ in Table 1 and depicted in Figure 2) we calculate a distinct hyperfine shift, ranging from ~3200 to ~3900 ppm. Shifts are inversely correlated with the Ni−$O_{ax}$ distance. Although distinct resonances cannot be resolved in our initial spin−echo mapped room-temperature spectrum, where all $O_{ax}$ sites appear within a single broad feature, the calculated hyperfine shift averaged among all axial sites (3539 ppm) is in good agreement with the experimental $O_{ax}$ shift of ~3500 ppm.

**Table 1. Calculated and Experimental Structural and $^{17}$O NMR Parameters (Computed Ni−O Bond Lengths, Experimental Isotropic Chemical Shifts $\delta_{iso,exptl}$, Calculated Fermi Contact Shifts $\delta_{FC,calcd}$, and Quadrupolar Coupling Constants $C_Q$) for $La_2NiO_{4+\delta}$ at Room Temperature[a]**

| | Ni−O dist. (Å) | $\delta_{iso,exptl}$ (ppm) | $\delta_{FC,calcd}$ (ppm) | $C_Q$ (MHz) exptl | $C_Q$ (MHz) calcd |
|---|---|---|---|---|---|
| $O_{eq}$ | ~1.9 (avg) | ~6500; 6860 (6) (MATPASS) | 10 322 | ≥4.6 | 4.73 |
| $O_{ax}$ | ~2.2 (avg) | ~3500 | 3539 (avg) | <4.6 | 1.14 (avg) |
| $O_{ax,0}$ | −[b] | 5590 (5) | −[b] | <4.6 | −[b] |
| $O_{ax,1}$ | 2.13 | 4775 (4) | 3914 | <4.6 | 2.35 |
| $O_{ax,2}$ | 2.16 | 4315 (3) | 3821 | <4.6 | 1.09 |
| $O_{ax,3}$ | 2.24 | 3960 (3) | 3234 | <4.6 | 0.67 |
| $O_{ax,4}$ | 2.26 | 3640 (2) | 3189 | <4.6 | 0.46 |
| $O_i$ | −[c] | 532 (1) | 19 | <4.6 | 0.38 |

[a]Standard errors in the fitted experimental shifts are given in parentheses. [b]Not observed in DFT-optimized supercell. [c]Not bonded to Ni.



DOI: 10.1021/jacs.6b07348
J. Am. Chem. Soc. 2016, 138, 11958−11969

The calculated shifts of the more distant equatorial oxygen sites are less influenced by the interstitial defect. In this case competing effects are at work: (1) a distribution of Ni−$O_{eq}$ bond lengths due to lattice distortion of the −Ni−$O_{eq}$−Ni− chains, and (2) differences in spin density transfer to $O_{eq}$ via the Ni $d_{x^2-y^2}$ orbital due to $Ni^{2/3+}$ charge ordering. Moreover, the range of calculated hyperfine shifts across all $O_{eq}$ sites is small relative to the average shift of ∼10 000 ppm. In short, $O_{eq}$ shifts do not cluster in distinct groups and, unlike the axial environments, cannot be easily classified by structural type. Nonetheless, the calculated hyperfine shift is much larger for $O_{eq}$ than $O_{ax}$, as expected, confirming the spectral assignment. The theoretical and experimental shifts for $O_{eq}$, however, differ by nearly 4000 ppm. This large discrepancy is not entirely unreasonable; theoretical calculations of $^{17}O$ hyperfine shifts in the solid state remain rudimentary, particularly at the level of hybrid DFT. Only Kong et al. have reported attempts for various paramagnetic coordination complexes, with results highly functional-dependent and with errors as large as 2500 ppm.[38] We believe the error is partly attributable to a nonoptimal choice of functional (Kong et al. describe errors of nearly 6000 ppm before selection of an appropriate functional), but ultimately derives from the self-interaction error in DFT that enables excessive spin density delocalization onto the nearby $O_{eq}$ sites.[81] We also note that the higher concentration of $Ni^{2+}$ in the theoretical supercell relative to experiment would increase the calculated $O_{eq}$ (but not $O_{ax}$) shift. Additionally, residual antiferromagnetic couplings within the perovskite layers could lead to lower-than-predicted experimental $O_{eq}$ shifts.

The interstitial site has a very small calculated hyperfine shift (of only 19 ppm), as expected, and hence the experimentally observed shift (of 532 ppm) is dominated by the chemical shift, not considered in these calculations.

Calculated quadrupolar coupling constants (Table 1) reflect the diversity of local charge and bonding asymmetry among oxygen environments. Typical values of $C_Q$ for $^{17}O$ nuclei in inorganic oxides vary from hundreds of kHz in highly symmetric alkaline earth oxides to 5−10 MHz in phosphates and chlorates;[82] here, calculated $C_Q$'s for $La_{16}Ni_8O_{33}$ span the known experimental range. The single interstitial oxygen site has a very nearly tetrahedral coordination to $La^{3+}$, and a correspondingly small $C_Q$ (0.38 MHz). By contrast, $O_{ax}$ sites possess an octahedrally coordinated geometry with five $La^{3+}$ and one $Ni^{2/3+}$. In this case the charge asymmetry (tri- vs bivalent neighboring cations), distorted bond angles, and the short Ni−$O_{ax}$ distance yield larger $C_Q$ values. Furthermore, the axial displacement generating a distribution of Ni−$O_{ax}$ bond lengths also yields distinct $C_Q$'s for each split $O_{ax}$ site, ranging from ∼0.5 to 2.4 MHz. Lastly, equatorial sites ($O_{eq}$) experience a locally octahedral environment as well, but with different neighbors: four $La^{3+}$ and two $Ni^{2/3+}$ in an axially compressed arrangement. Much shorter Ni−$O_{eq}$ distances (1.9 Å) relative to La−$O_{eq}$ (2.5−2.7 Å), combined with the effect of $NiO_6$ tilting distortions, give rise to a much larger $C_Q$ (4.73 MHz).

**3.4. Room-Temperature MATPASS NMR with Spectral Editing.** Suspecting from DFT calculations that additional spectral features could appear at higher resolution, we have performed further NMR experiments at faster magic-angle spinning (40 kHz). Spin−echo mapped spectra acquired at this spinning frequency now show evidence for overlapping spinning sidebands from additional sites (Figure 3, upper black trace). However, even with fast spinning, it is difficult to clarify details of the underlying fine structure due to spinning sideband overlap. The use of higher spinning speeds (e.g., 60 kHz) is unfortunately not feasible here, as the reduced sample volume would prohibitively increase acquisition time. Alternatively, experiments at lower magnetic field would increase the effective spectral distance between sidebands, improving resolution at a given spinning speed, but second-order quadrupolar effects would likely worsen resolution.

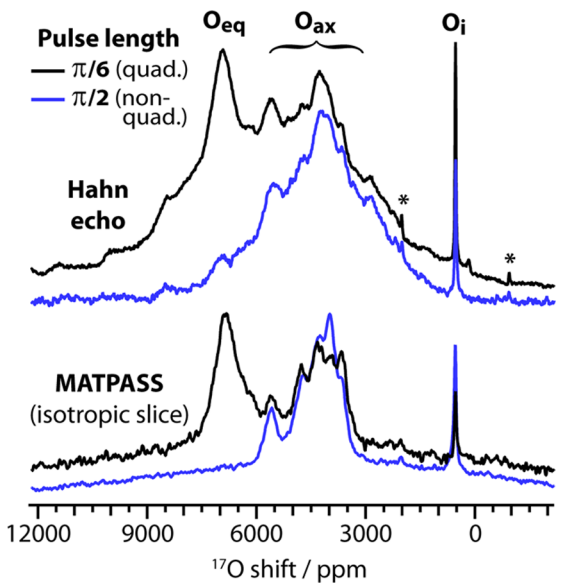


**Figure 3.** Comparison of Hahn echo and MATPASS NMR spectra of $La_2NiO_{4+\delta}$, with quadrupolar filtering. Spectra were acquired at 4.7 T with a MAS rate of 40 kHz. Splitting of $O_{ax}$ is partially resolved in the Hahn echo and fully resolved in the MATPASS data. Both experiments show pulse length dependence ($\pi/6$ vs $\pi/2$) consistent with a single highly quadrupolar environment ($O_{eq}$). Asterisks denote spinning sidebands where apparent.

We therefore turn to a method of spinning sideband separation, (projection) magic angle turning and phase-adjusted sideband separation, or MATPASS. This two-dimensional pulse sequence has been used by Hu et al. to obtain broadband "infinite"-MAS spectra in the case of large (>1 MHz) shift anisotropy.[83] The MATPASS experiment also succeeds in the familiar case of moderately quadrupolar nuclei ($^6Li$, $^7Li$) in paramagnetic environments.[53] Applying the technique to $^{17}O$-enriched $La_2NiO_{4+\delta}$ and extracting the isotropic slice (Figure 3, bottom black trace and Figure S6, inset) reveals six distinct paramagnetic features from ∼3500−7000 ppm, in addition to the usual peak at 532 ppm previously assigned to $O_i$.

Since the calculated hyperfine shifts from DFT (subsection 3.3) are not necessarily sufficiently accurate to discriminate among the different sites, we employ a form of spectral editing, quadrupolar filtering, exploiting the quadrupolar interaction to selectively suppress environments with large $C_Q$ to aid in the assignments. This approach hinges on $C_Q$-dependent differences in quadrupolar nutation behavior, wherein sites with quadrupolar frequencies $\upsilon_Q$ much larger than the rf field strength $\upsilon_1$ experience more efficient excitation by short rf pulses, on account of selective excitation of the central transition.[84] (For spin-5/2 nuclei, the quadrupolar frequency $\upsilon_Q$ is equal to $3C_Q/20$.) In practice, rf pulses with short flip angles will resolve all sites regardless of $C_Q$, whereas application of longer rf pulses (e.g., $\pi/2$ for a liquid reference) will


DOI: 10.1021/jacs.6b07348
J. Am. Chem. Soc. 2016, 138, 11958−11969

preferentially select small-$C_Q$ environments. Kentgens has shown that for spin-5/2 nuclei, a value of $\upsilon_Q \geq 6\upsilon_1$ is a reasonable threshold for full attenuation of signal using a longer, $\pi/2$ pulse (calibrated on a liquid reference).[77] In our case, where $\upsilon_1$ = 114 kHz, this corresponds to a threshold $C_Q$ of 4.6 MHz.

Repeating the MATPASS experiment using a longer $\pi/2$ pulse (bottom blue trace, Figure 3), we observe the loss of the paramagnetic feature centered at 6860 ppm; we conclude that the $C_Q$ of this site must equal or exceed 4.6 MHz. Among all DFT-calculated $C_Q$'s, only that of $O_{eq}$ (4.73 MHz) does so. On this basis, the furthest shifted feature is again assigned to $O_{eq}$. None of the other environments are fully attenuated by the longer rf pulse. Thus, the remaining five paramagnetic sites are all assigned to (distorted) $O_{ax}$ sites, for which $C_Q$ < 4.6 MHz (Table 1).

The five distinct $O_{ax}$ features resolved by MATPASS experiments are extremely suggestive of the split $O_{ax}$ sites obtained from DFT. Here, we do not necessarily imply that the experimental axial environments correspond to the geometries depicted in Figure 2, but rather that the presence of some form of axial displacement is consistent with the splitting of $O_{ax}$ features in the spectra. For completeness we "assign" four of the five experimental $O_{ax}$ features to the $O_{ax,1}$−$O_{ax,4}$ sites. The range of experimental and calculated hyperfine shifts is in reasonable agreement, though results from DFT underestimate the experimental values. The otherwise unassigned, highly shifted $O_{ax}$ feature at 5590 ppm (labeled $O_{ax,0}$ in Table 1) could correspond to a structural motif not considered in the DFT calculations, such as an axial oxygen with two nearby interstitials, which would experience a substantial displacement and much larger hyperfine shift. This assertion seems plausible given the higher experimental concentration of interstitials ($\delta$ = 0.15−0.17) compared to the DFT-optimized supercell ($\delta$ = 0.125). It is interesting that the $O_{ax}$ features cluster in well-defined peaks rather than display a broad continuum, suggesting a discrete set of Ni−$O_{ax}$ bond lengths, which may imply a degree of two-dimensional ordering of the interstitial defects. We can compare these results to the neutron diffraction study of Demourgues et al. of "$La_8Ni_4O_{17}$" ($\delta$ = 0.25), wherein eight $O_{ax}$ sites are identified, with five distinct Ni−$O_{ax}$ distances.[85]

Relative intensities of split $O_{ax}$ sites in the MATPASS spectra cannot be considered quantitative, as the apparent intensities are inversely weighted by dipolar broadening. That is, sites with large anisotropy have significant intensity distributed across the spinning sideband manifold and so appear smaller in the isotropic slice. The presence of residual spinning sidebands in the isotropic slice, as well as $T_2$ relaxation effects and the use of a very short recycle delay (50 ms) further complicate quantification. However, the presence of several split features in the spectra implies that most axial oxygens reside in slightly displaced environments.

As a conclusive check, the isotropic shifts obtained from MATPASS were used to model spinning sideband patterns that approximately reproduce the Hahn echo spectra recorded at 40 kHz, with both short ($\pi/6$) and long ($\pi/2$) rf pulse lengths (upper traces, Figure 3) as described in more detail in the SI (Figure S6).

**3.5. Variable-Temperature NMR (≤150 °C).** We hypothesize that the orthorhombic-to-tetragonal phase transition near 150 °C may be associated with changes in the local distortion of the $O_{ax}$ environments induced by motion of nearby $O_i$. To test this conjecture, we employ $^{17}$O VT-NMR as a probe of thermally activated oxygen motion in $La_2NiO_{4+\delta}$. As technical restrictions limit the concurrent use of fast MAS and sample heating, the following spectra have been acquired under slower spinning (12.5 kHz).

*Focus on Interstitial Site.* We first study the variable-temperature behavior of the interstitial oxide site at ∼535 ppm, choosing a field strength of 16.4 T. (This feature moves by ∼ +3 ppm at high field.) At such a large field, though the paramagnetic features ($O_{ax}$, $O_{eq}$) broaden and become difficult to separate, more spinning sidebands arise for the $O_i$ feature, potentially providing detailed information about the local geometry of this site.

Figure 4 shows the $^{17}$O MAS NMR spectra of the interstitial oxide site in $La_2NiO_{4+\delta}$ from room temperature to 134 °C. The most salient change in the spectra is a slight broadening and a loss of signal at and above 80 °C, especially between 94 and 107 °C (Figure 4a). At the highest temperature measured (134 °C), at most, 3% of the initial intensity remains. Concurrent with the loss of $O_i$ signal at 107 and 134 °C, a broad, asymmetric shoulder appears at a higher frequency of approximately 30 ppm, at 565 ppm (Figure 4b). The resonance falls between the pseudotetrahedral interstitial environment of $La_2NiO_{4+\delta}$ at 535 ppm and the tetrahedrally coordinated oxygen environment of $La_2O_3$ previously reported at 584 ppm.[71] Among $OLa_4$ sites with known $^{17}$O shifts (only $La_2NiO_{4+\delta}$ in this work, LaO(OH), and $La_2O_3$), the shift moves to higher frequency with reduction of the average O−La bond length and an increase in local tetrahedral symmetry.[86] A shift of 565 ppm is therefore suggestive of $OLa_4$ in a less stretched and distorted environment as compared to $O_i$ in $La_2NiO_{4+\delta}$, although not as symmetric as in $La_2O_3$. On this basis, we tentatively suggest that the feature at 565 ppm arises from $OLa_4$ sites in a slightly distorted $La_2O_3$ phase at the surface of the $La_2NiO_{4+\delta}$ particles. (This feature is not due to a separate bulk $La_2O_3$ phase, as the 584 ppm shift of $OLa_4$ in bulk $La_2O_3$ remains at this shift with increase in temperature; see Figure S15.) The existence of a La-enriched surface layer is consistent with reports on the unexpectedly strong preference for AO termination in $ABO_3$ perovskites, and has moreover been observed experimentally in $La_2NiO_{4+\delta}$ via SIMS-LEIS.[87,88] Lastly, on cooling to room temperature (red trace, Figure 4a), the $O_i$ signal returns at 535 ppm with, remarkably, nearly quantitative (98%) recovery of the original integrated intensity. We argue in subsection 4.1 that the intensity changes are consistent with a motional process involving the interstitial defects.

*Broadband Spectra.* To correlate the onset of interstitial motion with mechanistic details by probing temperature-dependent changes in the paramagnetic sites, we have recorded broadband spectra at similar temperatures. Here, a lower field strength (7.05 T), and thus narrower spectral width, ensures that some signal is recorded from all sites ($O_{eq}$, $O_{ax}$, and $O_i$) when acquiring from a single rf carrier frequency. This central-carrier approach obviates a time-consuming spin−echo mapping experiment, though also preventing quantitative comparison of intensities between different sites.

The broadband VT spectra (Figure 5) display a complex temperature-dependent behavior that, for convenience, we sequentially describe in terms of the diamagnetic region (near $O_i$), the near paramagnetic region (near $O_{ax}$), and the far paramagnetic region (near $O_{eq}$). A significant loss of intensity occurs across all sites with increasing temperature, such that the


DOI: 10.1021/jacs.6b07348
J. Am. Chem. Soc. 2016, 138, 11958−11969

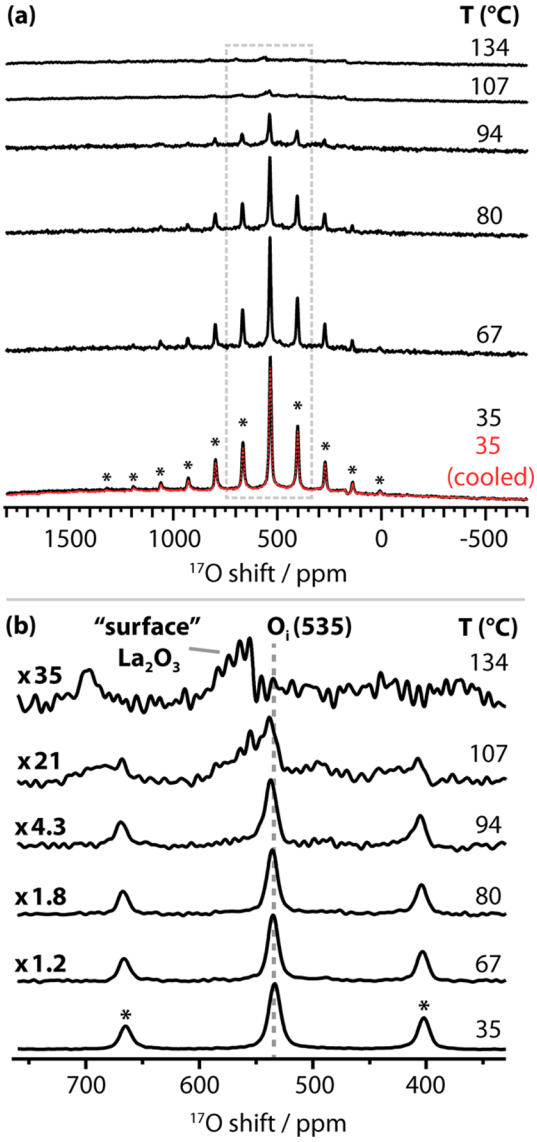


**Figure 4.** Variable-temperature NMR spectra of $La_2NiO_{4+\delta}$, focusing on the interstitial oxygen site. (a, top to bottom) $^{17}O$ MAS NMR spectra of $La_2NiO_{4+\delta}$ acquired at the indicated temperatures, and at 35 °C after cooling from high temperature (red). The difference between normal room temperature and the lowest sample temperature (35 °C) is due to frictional heating by MAS. Spectra were acquired at 16.4 T under a MAS rate of 12.5 kHz. Spectra shown are normalized to the number of scans. (b) Detail of (a) with spectra scaled to highlight broadening and shift of interstitial site. Asterisks denote spinning sidebands (for clarity shown only at 35 °C).

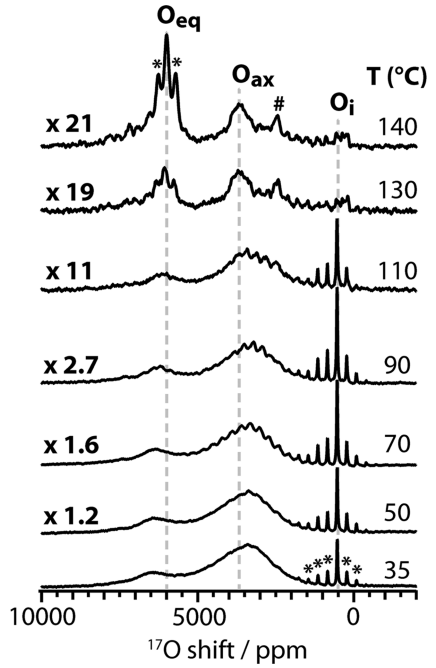


**Figure 5.** Broadband variable-temperature NMR spectra of $La_2NiO_{4+\delta}$. Spectra were acquired at 7.05 T at a MAS rate of 12.5 kHz. Spectra were normalized to number of scans (between ~300 000 and ~6 700 000 per spectrum) and then scaled as shown to obtain similar intensity for the $O_{ax}$ feature (~3500 ppm) present in all spectra. #Indicates the feature at 2400 ppm assigned to the $La_3Ni_2O_7$/$La_4Ni_3O_{10}$ impurity phase (see SI, section 5). Asterisks denote visible spinning sidebands, for clarity only indicated for $O_i$ at 35 °C and for $O_{eq}$ at 140 °C. (A close-up view of the spectrum at 140 °C depicting the weakly resolved peaks in the diamagnetic region is shown in Figure S9.)

spectra in Figure 5 are scaled arbitrarily to present similar overall signal strength.

In the diamagnetic region, signal from $O_i$ at 532 ppm decreases with increasing temperature. The absolute integrated intensity of $O_i$ shows a qualitatively similar loss as a function of temperature as seen at high field. As before, the $O_i$ feature vanishes in the high-temperature spectra (130 and 140 °C), revealing the 565 ppm shoulder near $O_i$. Weak features at 380 ppm ($ZrO_2$ sample holder[89]) and 170 ppm ($LaAlO_3$ impurity) are also rendered more obvious at these temperatures in the absence of overlap by spinning sidebands of $O_i$ (see Figure S9).

The near paramagnetic region at modest temperatures (to 110 °C) shows a moderate loss of signal at $O_{ax}$, which is slightly more pronounced than that for $O_i$, concurrent with the appearance of spinning sidebands on top of the broad underlying paramagnetic feature. The positions of these spinning sidebands are highly temperature-dependent, and they are not associated with the fixed-position $O_i$ feature. Above 110 °C, a major narrowing of the $O_{ax}$ site occurs, centering the shift at 3650 ppm, and revealing a minor feature at 2400 ppm. Moreover, small spinning sidebands associated with this latter feature appear at lower frequencies (between 2200 and 800 ppm).

Finally, the far paramagnetic region is characterized by a decrease in intensity but very little change in the line shape until above 110 °C, where the $O_{eq}$ site suddenly sharpens and grows in intensity relative to $O_{ax}$. This narrowing is so profound that, at 140 °C, spinning sidebands flank either side of the isotropic shift, and the apparent isotropic shift also moves to lower frequency (6000 ppm). Higher-frequency features are observed out to 8000 ppm and are approximately spaced at the MAS rate relative to the $O_{eq}$ isotropic shift indicating that they correspond to the satellite transitions of $O_{eq}$.

## 4. DISCUSSION

**4.1. Kinetics of Interstitial Motion.** One can postulate several reasons for the dramatic loss of the interstitial feature on heating (Figure 4), such as changes in the Boltzmann distribution of spin states or the physical removal (outgassing) of $^{17}O$ as $O_2$. The first case proves unlikely, as a decrease in the population difference of the central transition spin states on


DOI: 10.1021/jacs.6b07348
J. Am. Chem. Soc. 2016, 138, 11958−11969

heating from 35 to 134 °C (308 to 407 K) can only diminish the signal by at most about 25% (as the spin population difference varies essentially linearly with temperature). Notably, the previously assigned $LaAlO_3$ impurity feature at 170 ppm retains the majority of its intensity with increase in temperature (Figure S8), which is consistent with this. We also discount the gaseous elimination of $^{17}O$ at elevated temperature, because the recovery of the original spectrum on cooling suggests that the post-VT sample remains comparably $^{17}O$-enriched.

Instead, we propose that the spectral changes in Figure 4 are consistent with the onset of oxide-ion dynamics on the NMR time scale, namely, exchange between the interstitial site and a paramagnetic oxygen environment. In an ideal, thermally activated two-site exchange, as the exchange rate increases, the two spectral features broaden and eventually coalesce. Furthermore, rapid exchange enhances spin dephasing and leads to greatly reduced $T_2$ relaxation times. This in turn induces significant loss of spectral intensity in multiple-pulse NMR sequences such as the Hahn echo experiments performed here.

Assuming thermally activated (Arrhenius-type) exchange, in the so-called slow motion or "visit-limited" regime of the Meiboom chemical exchange model,[90,91]

$$\log I = \log I_0 - \frac{2\tau}{c} A_0 [\exp(-1/T)]^{E_a/R} \quad (3)$$

where $I$ is the integrated signal intensity as observed experimentally, $T$ is the sample temperature, $E_a$ is the activation energy, and the other variables are experimental constants or proportionality constants: $I_0$ is the integrated signal intensity from a one-pulse experiment, $\tau$ is the (fixed) rotor period, $c = k_{ex}T_2$ (where $k_{ex}$ is the exchange rate), $A_0$ is the Arrhenius pre-exponential factor, and $R$ is the gas constant. (For derivation and further details see SI, section 3.) Analyzing the loss of integrated $O_i$ intensity in this way (after first subtracting the intensity belonging to the surface $OLa_4$ sites at 565 ppm), we extract an $E_a$ for interstitial motion equal to 0.59 ± 0.07 eV (see SI, section 3 and Figure S11). This result agrees well with the MD−simulated value of 0.51 eV given by Chroneos et al. for exchange between axial and interstitial sites,[45] as well as a value of 0.54 eV for oxygen self-diffusion in polycrystalline $La_2NiO_{4+\delta}$ as determined by TOF-SIMS.[92] We thus assign this motional process to interstitial−axial exchange. We note, however, that our activation energy is calculated over a much lower temperature range (<134 °C) than in the previous literature (350−700 °C).

Asymmetric two-site exchange simulations[93] (Figure S12) were performed to explore the effect of exchange between the interstitial and axial anions on the observed lineshapes. We estimate a conservative upper bound $k_{ex}$ < 320 kHz for this process, with the correlation time for interstitial jumps no shorter than 3.2 $\mu$s, at 134 °C.

**4.2. Analysis of Broadband Variable-Temperature Spectra.** The complex line shape changes in the paramagnetic features (Figure 5) allow us to explore the onset of oxygen motion in the context of the reported orthorhombic−tetragonal phase transition near 150 °C. The most prominent change in the spectra is the sudden narrowing of the $O_{eq}$ feature at 130 °C, which suggests a much smaller distribution of isotropic, time-averaged hyperfine shifts. The further increase in the $O_{eq}$ centerband intensity at 140 °C also indicates a significant lessening of sources of spectral anisotropy such as electron−nuclear dipolar broadening. We assign the $O_{eq}$ line shape changes to the rocking motion of $NiO_6$ octahedra entering the fast motion regime at, or nearly at, the phase transition temperature. On the basis of the maximum frequency separation between $O_{eq}$ sites of ∼2000 ppm ≈ 82 kHz seen at room temperature, we calculate that the motional rate of rocking exceeds 180 kHz ($= \pi/\sqrt{2} \times 82$ kHz)[94] at 130 °C.

The previous neutron diffraction study by Skinner has also resolved a significant loss of anisotropy of the equatorial oxygen site near the phase transition temperature.[41] In that work, the $O_{eq}$ thermal factors at 25 °C show a significant $c$-axis displacement ($U_{33}/U_{11} \approx 2$, $U_{33}/U_{22} \approx 5$), similar to the out-of-plane equatorial distortion depicted in Figure 2. At and above 150 °C, however, the $O_{eq}$ thermal ellipsoid appears isotropic. Here, the VT-NMR spectra corroborate the collapse of the $O_{eq}$ environment to an isotropic (in-plane) environment at these temperatures, consistent with fast rocking of the $NiO_6$ octahedra.

The $O_{ax}$ site similarly narrows at and above 130 °C (Figure 5) to a feature approximately at the average of the distorted $O_{ax}$ environments resolved by MATPASS experiments (shown in Figure 3), which suggests a time-averaging of the mean $O_{ax}$ distortion. We attribute this change to a similar motional mechanism, i.e. local rocking of $NiO_6$ octahedra, while noting that simultaneous exchange with interstitial sites competes by contributing to broadening of this site (relative to $O_{eq}$, which does not exchange at these temperatures). Furthermore, the $O_{ax}$ dynamics are likely subject to a distribution of motional correlation times. The presence of spinning sidebands at lower temperatures (∼70 °C), for example, suggests a partial averaging of a subset of the distorted $O_{ax}$ environments by motion already in the fast exchange limit. In previous VT-NMR studies of anionic conductors, the coexistence of multiple correlation times has been attributed to vacancy−dopant ordering or to the presence of mobile and rigid domains with differing defect concentrations.[18,95] In this system, the apparent variation in $O_{ax}$ motional rates likely results from the larger population of axial sites relative to that of the interstitial defects with which they exchange.[96]

The influence of interstitial motion on the dynamics of the $O_{ax}$ and $O_{eq}$ sites can be inferred in several ways. We note that the calculated motional rate of $NiO_6$ rocking (in excess of 180 kHz) is near the coalescence regime for interstitial−axial exchange (Figure S12), suggesting that near the phase transition temperature, the exchange motion is coupled to the octahedral rocking (or vice versa). Second, clearly shown in the DFT calculations, and experimentally from the distribution of shifts, the $O_{ax}$ distortion arises from proximity to interstitial defects, and therefore the long-range motion of interstitials necessarily contributes to averaging of the $O_{ax}$ distortion. We conclude that the loss, or significant reduction of, the local $O_i$-induced distortion occurs at or near the phase transition and is moreover correlated with exchange between interstitial and axial sites.

**4.3. Extension to Other Systems and Higher Temperatures.** The VT-NMR results clarify that the previously observed orthorhombic−tetragonal phase transition arises from the loss of a local structural distortion that is correlated with rapid oxide-ion dynamics. It remains unclear how this distortion leads to the cooperative tilting of perovskite layers in the bulk and thus the low-temperature orthorhombic structure, but we note that even for very subtle phase transitions, VT-NMR spectra should resolve the relevant motional changes that drive the transition. An example system is the related phase


DOI: 10.1021/jacs.6b07348
J. Am. Chem. Soc. 2016, 138, 11958−11969

$La_2NiO_{4.11-4.13}$, which undergoes a subtle transition at ~300 K with both low- and high-temperature phases nominally tetragonal, but with long-range 3D interstitial ordering only apparent below 300 K.[97] The sensitivity of the NMR spectra could in this case provide a convenient check on the interplay of oxygen motion and interstitial ordering, even where the latter property is not readily apparent by diffraction or other techniques.

Work is in progress to acquire and assign high-temperature (150 °C−800 °C) $^{17}O$ NMR spectra of $La_2NiO_{4+\delta}$ to explore motion involving exchange between all of the oxygen sites and to examine the effect of temperature on oxygen interstitial content.

## 5. CONCLUSION

A combined experimental (NMR spectroscopy) and computational (DFT) methodology has been employed to clarify the local structure and dynamics of the mixed ionic−electronic conductor $La_2NiO_{4+\delta}$ by obtaining $^{17}O$ MAS NMR spectra of this paramagnetic oxide in the solid state. Our main conclusions are as follows:

(1) Small compositional changes in $La_2NiO_{4+\delta}$ occur as a result of $^{17}O$-enrichment; we observe an increase in the oxygen excess (before: $\delta$ = 0.12−0.14; after: $\delta$ = 0.15−0.17 by XRD, $\delta$ = ~0.2 by quantitative NMR) and the formation of small amounts (~3 wt %) of an impurity assigned to the higher-order $La_4Ni_3O_{10}$ phase.

(2) Room-temperature $^{17}O$ MAS NMR spectra of $^{17}O$-enriched $La_2NiO_{4+\delta}$ acquired by spin−echo mapping reveal three distinct oxygen environments assigned to interstitial ($O_i$), axial ($O_{ax}$) and equatorial ($O_{eq}$) sites, with quantitative measurements suggesting fully stochastic $^{17}O$-enrichment.

(3) DFT calculations of $La_2NiO_{4+\delta}$ provide local structural insight and are used to obtain Fermi contact (hyperfine) shifts and quadrupolar coupling constants that corroborate the assignment of the experimental spectra. In particular, paramagnetic $O_{eq}$ and $O_{ax}$ features can be distinguished on the basis of the much larger $C_Q$ of the former (4.7 MHz vs ~1.1 MHz).

(4) High-resolution MATPASS NMR spectra, in combination with quadrupolar filtering techniques, reveal the splitting of the $O_{ax}$ site into five discrete axial environments (3640−5590 ppm). Our DFT calculations also show a similar clustering of four distinct $O_{ax}$ shifts, which can be rationalized on the basis of Ni−$O_{ax}$ distances. We demonstrate that this axial splitting arises from a local structural distortion directly induced by the interstitial defect.

(5) Variable-temperature NMR spectra at high field resolve the (reversible) loss of the interstitial oxide feature due to a thermally activated motional process with $E_a$ = 0.59 ± 0.07 eV; we assign this motion to exchange with axial sites.

(6) Analysis of the entire broadband spectrum as a function of temperature allows us to elucidate the types of motion and exchange affecting the interstitial, axial, and equatorial oxygen sites. In brief, exchange between interstitial and axial sites dominates the intensity loss of the $O_i$ resonance. Local rocking motion of $NiO_6$ octahedra, with associated averaging effects on axial and equatorial displacement, is dominant for the $O_{ax}$ and $O_{eq}$ lineshapes, with a motional rate larger than 180 kHz at 130 °C. Abrupt changes in the VT-NMR spectra are associated with approach to the previously reported orthorhombic-to-tetragonal phase transition of $La_2NiO_{4+\delta}$, these changes occurring here between 110 and 130 °C. We observe a significant reduction in the magnitude of local structural distortions due to $NiO_6$ octahedral motion, correlated with interstitial−axial exchange, at the phase transition temperature; this illustrates how oxide-ion motion at the atomic level directly influences the phase transition in the bulk.

The design of next-generation MIECs with improved oxide-ion conductivity relies on a fundamental understanding of the underlying anion dynamics across a wide temperature range, which $^{17}O$ VT-NMR spectroscopy is uniquely poised to resolve. Work is ongoing to obtain high-temperature spectra (>150 °C) of $La_2NiO_{4+\delta}$ to provide insight into oxygen conduction mechanisms in the conditions most relevant for IT-SOFC and sensor operation. We also anticipate that cation doping of perovskite MIECs, a common strategy in tuning material properties such as the electronic and ionic conductivity, will have significant effects on the paramagnetic $^{17}O$ spectra and allow for comprehensive depictions of the local structure and dynamics, as well as the fundamental defect chemistry, of these functionally relevant oxides.

## ■ ASSOCIATED CONTENT

### Supporting Information

The Supporting Information is available free of charge on the ACS Publications website at DOI: 10.1021/jacs.6b07348.

Powder XRD patterns of $La_2NiO_{4+\delta}$ and of mixed samples of $La_2NiO_{4+\delta}$, NiO, $La_3Ni_2O_7$ and $La_4Ni_3O_{10}$; TGA data under reducing conditions and correlation of TGA-determined oxygen excess ($\delta$) with refined lattice parameters; details of computational methods with depictions of DFT-optimized supercells; details of determining activation energy ($E_a$) of interstitial motion; description of origin of the local axial distortion; quantitative fitting and deconvolution of Hahn echo and MATPASS NMR spectra; close-up of high-temperature broadband NMR spectra of $La_2NiO_{4+\delta}$; $^{17}O$ NMR spectra of mixed sample of $La_2NiO_{4+\delta}$, $La_3Ni_2O_7$ and $La_4Ni_3O_{10}$; calculation of phase fractions of surface $La_2O_3$ and $La_3Ni_2O_7/La_4Ni_3O_{10}$ impurity; temperature- and sample-dependent intensity of $LaAlO_3$ impurity; temperature dependence of $^{17}O$ NMR shifts of $La_2O_3$; and asymmetric interstitial−axial exchange simulations (PDF)

## ■ AUTHOR INFORMATION


### Corresponding Author

*cpg27@cam.ac.uk

### Present Address

‖R.D.: Institute for Molecules and Materials, Radboud University, Heyendaalseweg 135, 6525 AJ Nijmegen, The Netherlands.


### Notes

The authors declare no competing financial interest.

Data supporting this work are available from www.repository.cam.ac.uk.

## ■ ACKNOWLEDGMENTS

Via membership of the U.K.'s HPC Materials Chemistry Consortium, some computations have made use of ARCHER, the U.K.'s national high-performance computing service, which is funded by the Office of Science and Technology through EPSRC's High End Computing Programme (EPSRC Grant No. EP/L000202). This research also used resources of the



DOI: 10.1021/jacs.6b07348
J. Am. Chem. Soc. 2016, 138, 11958−11969

Center for Functional Nanomaterials, which is a U.S. DOE Office of Science Facility, at Brookhaven National Laboratory under Contract No. DE-SC0012704. D.M.H. acknowledges funding from the Cambridge Commonwealth Trusts. C.P.G. and G.K. thank the European Research Council for an Advanced Fellowship [grant agreement No. 247411]. F.B. thanks the EU Marie Curie actions for an International Incoming Fellowship 2011−2013 (Grant 275212) and Clare Hall, University of Cambridge, for a Research Fellowship. Sylvia Britto, Evan Keyzer, Alexander C. Forse, Beth Howe, Oliver Pecher, Raphaële J. Clément, George Lane, Ieuan Seymour, Luke Sperrin, and Michael W. Gaultois are acknowledged for useful discussions and support. Additional thanks are due to Michal Leskes (Weizmann Institute of Science) and Andrew J. Pell (Stockholm University) for assistance regarding NMR pulse sequences.

## REFERENCES

(1) Skinner, S. J. *Int. J. Inorg. Mater.* **2001**, *3*, 113−121.
(2) Tarancón, A.; Burriel, M.; Santiso, J.; Skinner, S. J.; Kilner, J. A. *J. Mater. Chem.* **2010**, *20*, 3799.
(3) Haugsrud, R.; Norby, T. *Nat. Mater.* **2006**, *5*, 193−196.
(4) Yang, L.; Wang, S.; Blinn, K.; Liu, M.; Liu, Z.; Cheng, Z.; Liu, M. *Science* **2009**, *326*, 126−129.
(5) Sengodan, S.; Choi, S.; Jun, A.; Shin, T. H.; Ju, Y.-W.; Jeong, H. Y.; Shin, J.; Irvine, J. T. S.; Kim, G. *Nat. Mater.* **2015**, *14*, 205−209.
(6) Sunarso, J.; Baumann, S.; Serra, J. M.; Meulenberg, W. A.; Liu, S.; Lin, Y. S.; Diniz da Costa, J. C. *J. Membr. Sci.* **2008**, *320*, 13−41.
(7) Luo, H.; Efimov, K.; Jiang, H.; Feldhoff, A.; Wang, H.; Caro, J. *Angew. Chem., Int. Ed.* **2011**, *50*, 759−763.
(8) Huang, K.; Wan, J.; Goodenough, J. B. *J. Mater. Sci.* **2001**, *36*, 1093−1098.
(9) Shao, Z.; Haile, S. M. *Nature* **2004**, *431*, 170−173.
(10) Tuller, H. L. *Solid State Ionics* **1997**, *94*, 63−74.
(11) Chroneos, A.; Yildiz, B.; Tarancón, A.; Parfitt, D.; Kilner, J. A. *Energy Environ. Sci.* **2011**, *4*, 2774−2789.
(12) Linford, R. G.; Hackwood, S. *Chem. Rev.* **1981**, *81*, 327−364.
(13) Reichert, D. *Annu. Rep. NMR Spectrosc.* **2005**, *55*, 159−203.
(14) Blanc, F.; Spencer, L.; Goward, G. R. *Encyclopedia of Magnetic Resonance: Quadrupolar NMR of Ionic Conductors, Batteries, and Other Energy-related Materials*; Harris, R. K., Ed.; John Wiley & Sons, Ltd: Chichester, UK, 2007.
(15) O'Dell, L. A.; Ratcliffe, C. I. *Encyclopedia of Magnetic Resonance: Quadrupolar NMR to Investigate Dynamics in Solid Materials*; Harris, R. K., Ed.; John Wiley & Sons, Ltd: Chichester, UK, 2007.
(16) Kim, N.; Grey, C. P. *Science* **2002**, *297*, 1317−1320.
(17) Kim, N.; Grey, C. P. *Dalton Trans.* **2004**, 3048−3052.
(18) Kim, N.; Vannier, R.-N.; Grey, C. P. *Chem. Mater.* **2005**, *17*, 1952−1958.
(19) Holmes, L.; Peng, L.; Heinmaa, I.; O'Dell, L. A.; Smith, M. E.; Vannier, R.-N.; Grey, C. P. *Chem. Mater.* **2008**, *20*, 3638−3648.
(20) Blanc, F.; Middlemiss, D. S.; Buannic, L.; Palumbo, J. L.; Farnan, I.; Grey, C. P. *Solid State Nucl. Magn. Reson.* **2012**, *42*, 87−97.
(21) Kim, G.; Griffin, J. M.; Blanc, F.; Haile, S. M.; Grey, C. P. *J. Am. Chem. Soc.* **2015**, *137*, 3867−3876.
(22) Fuda, K.; Kishio, K.; Yamauchi, S.; Fueki, K.; Onoda, Y. *J. Phys. Chem. Solids* **1984**, *45*, 1253−1257.
(23) Spearing, D. R.; Farnan, I.; Stebbins, J. F. *Phys. Chem. Miner.* **1992**, *19*, 307−321.
(24) Adler, S.; Russek, S.; Reimer, J.; Fendorf, M.; Stacy, A.; Huang, Q.; Santoro, A.; Lynn, J.; Baltisberger, J.; Werner, U. *Solid State Ionics* **1994**, *68*, 193−211.
(25) Witschas, M.; Eckert, H.; Freiheit, H.; Putnis, A.; Korus, G.; Jansen, M. *J. Phys. Chem. A* **2001**, *105*, 6808−6816.
(26) Hampson, M. R.; Evans, J. S. O.; Hodgkinson, P. *J. Am. Chem. Soc.* **2005**, *127*, 15175−15181.
(27) Kim, N.; Hsieh, C.-H.; Huang, H.; Prinz, F. B.; Stebbins, J. F. *Solid State Ionics* **2007**, *178*, 1499−1506.
(28) Buzlukov, A.; Trokiner, A.; Kozhevnikov, V.; Verkhovskii, S.; Yakubovsky, A.; Leonidov, I.; Gerashenko, A.; Stepanov, A.; Baklanova, I.; Tankeyev, A. *J. Solid State Chem.* **2011**, *184*, 36−43.
(29) Kiyono, H.; Matsuda, Y.; Shimada, T.; Ando, M.; Oikawa, I.; Maekawa, H.; Nakayama, S.; Ohki, S.; Tansho, M.; Shimizu, T.; Florian, P.; Massiot, D. *Solid State Ionics* **2012**, *228*, 64−69.
(30) Chien, P.-H.; Jee, Y.; Huang, C.; Dervişoğlu, R.; Hung, I.; Gan, Z.; Huang, K.; Hu, Y.-Y. *Chem. Sci.* **2016**, *7*, 3667−3675.
(31) Dervişoğlu, R.; Middlemiss, D. S.; Blanc, F.; Lee, Y.-L.; Morgan, D.; Grey, C. P. *Chem. Mater.* **2015**, *27*, 3861−3873.
(32) Seymour, I. D.; Middlemiss, D. S.; Halat, D. M.; Trease, N. M.; Pell, A. J.; Grey, C. P. *J. Am. Chem. Soc.* **2016**, *138*, 9405−9408.
(33) Blanc, F.; Middlemiss, D. S.; Gan, Z.; Grey, C. P. *J. Am. Chem. Soc.* **2011**, *133*, 17662−17672.
(34) Martel, L.; Magnani, N.; Vigier, J.-F.; Boshoven, J.; Selfslag, C.; Farnan, I.; Griveau, J.-C.; Somers, J.; Fanghänel, T. *Inorg. Chem.* **2014**, *53*, 6928−6933.
(35) Looyestijn, W. J.; Klaassen, T. O.; Poulis, N. J. *Physica B+C* **1978**, *93*, 349−357.
(36) Jurkutat, M.; Rybicki, D.; Sushkov, O. P.; Williams, G. V. M; Erb, A.; Haase, J. *Phys. Rev. B: Condens. Matter Mater. Phys.* **2014**, *90*, 140504.
(37) Bert, F.; Olariu, A.; Zorko, A.; Mendels, P.; Trombe, J. C.; Duc, F.; Vries, M. A. de; Harrison, A.; Hillier, A. D.; Lord, J.; Amato, A.; Baines, C. *J. Phys. Conf. Ser.* **2009**, *145*, 012004.
(38) Kong, X.; Terskikh, V. V.; Khade, R. L.; Yang, L.; Rorick, A.; Zhang, Y.; He, P.; Huang, Y.; Wu, G. *Angew. Chem., Int. Ed.* **2015**, *54*, 4753−4757.
(39) Woolley, R. J.; Skinner, S. J. *J. Power Sources* **2013**, *243*, 790−795.
(40) Demourgues, A.; Wattiaux, A.; Grenier, J. C.; Pouchard, M.; Soubeyroux, J. L.; Dance, J. M.; Hagenmuller, P. *J. Solid State Chem.* **1993**, *105*, 458−468.
(41) Skinner, S. J. *Solid State Sci.* **2003**, *5*, 419−426.
(42) Tavares, C. P. *Mater. Res. Bull.* **1985**, *20*, 979−987.
(43) Ganguly, P.; Rao, C. N. R. *J. Solid State Chem.* **1984**, *53*, 193−216.
(44) Aguadero, A.; Alonso, J. A.; Martínez-Lope, M. J.; Fernández-Díaz, M. T.; Escudero, M. J.; Daza, L. *J. Mater. Chem.* **2006**, *16*, 3402−3408.
(45) Chroneos, A.; Parfitt, D.; Kilner, J. A.; Grimes, R. W. *J. Mater. Chem.* **2010**, *20*, 266−270.
(46) Sayer, M.; Odier, P. *J. Solid State Chem.* **1987**, *67*, 26−36.
(47) Tamura, H.; Hayashi, A.; Ueda, Y. *Phys. C* **1993**, *216*, 83−88.
(48) Zhang, H. L.; Wu, X. S.; Chen, C. S.; Liu, W. *Phys. Rev. B: Condens. Matter Mater. Phys.* **2005**, *71*, 064422.
(49) Liu, T.; Xu, Y.; Li, Y.; Wang, Z.; Zhao, J. *Ceram. Int.* **2011**, *37*, 3361−3364.
(50) Larson, A. C.; Von Dreele, R. B. *General Structure Analysis System (GSAS)*; Los Alamos National Laboratory Report LAUR 86-748; Los Alamos National Laboratory: Los Alamos, NM, 2000.
(51) Toby, B. H. *J. Appl. Crystallogr.* **2001**, *34*, 210−213.
(52) Boehm, E.; Bassat, J.-M.; Steil, M. C.; Dordor, P.; Mauvy, F.; Grenier, J.-C. *Solid State Sci.* **2003**, *5*, 973−981.
(53) Hung, I.; Zhou, L.; Pourpoint, F.; Grey, C. P.; Gan, Z. *J. Am. Chem. Soc.* **2012**, *134*, 1898−1901.
(54) Bielecki, A.; Burum, D. P. *J. Magn. Reson., Ser. A* **1995**, *116*, 215−220.
(55) Beckmann, P. A.; Dybowski, C. *J. Magn. Reson.* **2000**, *146*, 379−380.
(56) *Topspin 3.2, software for NMR spectral analysis*; Bruker Biospin: Rheinstetten, Germany, 2012.
(57) Massiot, D.; Fayon, F.; Capron, M.; King, I.; Le Calvé, S.; Alonso, B.; Durand, J.-O.; Bujoli, B.; Gan, Z.; Hoatson, G. *Magn. Reson. Chem.* **2002**, *40*, 70−76.
(58) Dovesi, R.; Saunders, V. R.; Roetti, C.; Orlando, R.; Zicovich-Wilson, C. M.; Pascale, F.; Civalleri, B.; Doll, K.; Harrison, N. M.;


DOI: 10.1021/jacs.6b07348
J. Am. Chem. Soc. 2016, 138, 11958−11969

Bush, I. J. *CRYSTAL09 User's Manual*; University of Torino: Torino, Italy, 2010.
(59) Winkler, E.; Rivadulla, F.; Zhou, J.-S.; Goodenough, J. B. *Phys. Rev. B: Condens. Matter Mater. Phys.* **2002**, *66*, 094418.
(60) Pyykkö, P. *Mol. Phys.* **2008**, *106*, 1965−1974.
(61) Kim, J.; Middlemiss, D. S.; Chernova, N. A.; Zhu, B. Y. X.; Masquelier, C.; Grey, C. P. *J. Am. Chem. Soc.* **2010**, *132*, 16825−16840.
(62) Zhang, Y.; Castets, A.; Carlier, D.; Ménétrier, M.; Boucher, F. *J. Phys. Chem. C* **2012**, *116*, 17393−17402.
(63) Ganguly, P.; Kollai, S.; Rao, C. N. R. *Magn. Lett.* **1980**, *1*, 107.
(64) Goodenough, J. B.; Ramasesha, S. *Mater. Res. Bull.* **1982**, *17*, 383−390.
(65) Aguadero, A.; Pérez, M.; Alonso, J. A.; Daza, L. *J. Power Sources* **2005**, *151*, 52−56.
(66) Rice, D. E.; Buttrey, D. J. *J. Solid State Chem.* **1993**, *105*, 197−210.
(67) Tamura, H.; Hayashi, A.; Ueda, Y. *Phys. C* **1996**, *258*, 61−71.
(68) Sayers, R.; Skinner, S. J. *J. Mater. Chem.* **2011**, *21*, 414−419.
(69) Massiot, D.; Farnan, I.; Gautier, N.; Trumeau, D.; Trokiner, A.; Coutures, J. P. *Solid State Nucl. Magn. Reson.* **1995**, *4*, 241−248.
(70) Pell, A. J.; Clément, R. J.; Grey, C. P.; Emsley, L.; Pintacuda, G. *J. Chem. Phys.* **2013**, *138*, 114201.
(71) Yang, S.; Shore, J.; Oldfield, E. *J. Magn. Reson.* **1992**, *99*, 408−412.
(72) Jorgensen, J. D.; Dabrowski, B.; Pei, S.; Richards, D. R.; Hinks, D. G. *Phys. Rev. B: Condens. Matter Mater. Phys.* **1989**, *40*, 2187−2199.
(73) Bastow, T. J.; Dirken, P. J.; Smith, M. E.; Whitfield, H. J. *J. Phys. Chem.* **1996**, *100*, 18539−18545.
(74) Nordenskiold, L.; Laaksonen, A.; Kowalewski, J. *J. Am. Chem. Soc.* **1982**, *104*, 379−382.
(75) Oldfield, E.; Coretsopoulos, C.; Yang, S.; Reven, L.; Lee, H. C.; Shore, J.; Han, O. H.; Ramli, E.; Hinks, D. *Phys. Rev. B: Condens. Matter Mater. Phys.* **1989**, *40*, 6832−6849.
(76) Went, M. S.; Reimer, J. A. *Chem. Mater.* **1990**, *2*, 389−394.
(77) Kentgens, A. P. M. *Geoderma* **1997**, *80*, 271−306.
(78) Massiot, D.; Bessada, C.; Coutures, J. P.; Taulelle, F. *J. Magn. Reson.* **1990**, *90*, 231−242.
(79) Frayret, C.; Villesuzanne, A.; Pouchard, M. *Chem. Mater.* **2005**, *17*, 6538−6544.
(80) Takeda, Y.; Kanno, R.; Sakano, M.; Yamamoto, O.; Takano, M.; Bando, Y.; Akinaga, H.; Takita, K.; Goodenough, J. B. *Mater. Res. Bull.* **1990**, *25*, 293−306.
(81) Seo, D.-H.; Lee, J.; Urban, A.; Malik, R.; Kang, S.; Ceder, G. *Nat. Chem.* **2016**, *8*, 692−697.
(82) Gerothanassis, I. P. *Prog. Nucl. Magn. Reson. Spectrosc.* **2010**, *57*, 1−110.
(83) Hu, Y.-Y.; Levin, E. M.; Schmidt-Rohr, K. *J. Am. Chem. Soc.* **2009**, *131*, 8390−8391.
(84) Kentgens, A. P. M. *Encyclopedia of Magnetic Resonance: Quadrupolar Nutation Spectroscopy*; Harris, R. K., Ed.; John Wiley & Sons, Ltd: Chichester, UK, 2007.
(85) Demourgues, A.; Weill, F.; Darriet, B.; Wattiaux, A.; Grenier, J. C.; Gravereau, P.; Pouchard, M. *J. Solid State Chem.* **1993**, *106*, 317−329.
(86) Ali, F.; Smith, M. E.; Steuernagel, S.; Whitfield, H. J. *J. Mater. Chem.* **1996**, *6*, 261−264.
(87) Druce, J.; Téllez, H.; Burriel, M.; Sharp, M. D.; Fawcett, L. J.; Cook, S. N.; McPhail, D. S.; Ishihara, T.; Brongersma, H. H.; Kilner, J. A. *Energy Environ. Sci.* **2014**, *7*, 3593−3599.
(88) Wu, J.; Pramana, S. S.; Skinner, S. J.; Kilner, J. A.; Horsfield, A. P. *J. Mater. Chem. A* **2015**, *3*, 23760−23767.
(89) Bastow, T. J.; Stuart, S. N. *Chem. Phys.* **1990**, *143*, 459−467.
(90) Meiboom, S. *J. Chem. Phys.* **1961**, *34*, 375−388.
(91) Brooks, R. A. *Magn. Reson. Med.* **2002**, *47*, 388−391.
(92) Sayers, R.; De Souza, R. A.; Kilner, J. A.; Skinner, S. J. *Solid State Ionics* **2010**, *181*, 386−391.
(93) Bain, A. D. *MEXICO: The McMaster Program for Exchange Lineshape Calculations*; McMaster University, Hamilton, Ont., Canada, 2002.
(94) Bain, A. D. *Prog. Nucl. Magn. Reson. Spectrosc.* **2003**, *43*, 63−103.
(95) Wang, F.; Grey, C. P. *J. Am. Chem. Soc.* **1998**, *120*, 970−980.
(96) Adler, S. B.; Smith, J. W.; Reimer, J. A. *J. Chem. Phys.* **1993**, *98*, 7613−7620.
(97) Tranquada, J. M.; Kong, Y.; Lorenzo, J. E.; Buttrey, D. J.; Rice, D. E.; Sachan, V. *Phys. Rev. B: Condens. Matter Mater. Phys.* **1994**, *50*, 6340.


DOI: 10.1021/jacs.6b07348
*J. Am. Chem. Soc.* 2016, 138, 11958−11969